Materials and Design 150 (2018) 171–181

Contents lists available at ScienceDirect

Materials and Design

journal homepage: www.elsevier.com/locate/matdes

Mechanism of heat affected zone cracking in Ni-based superalloy DZ125L fabricated by laser 3D printing technique

Yao Li [a,b], Kai Chen [a,*], Nobumichi Tamura [b]

[a] Center for Advancing Materials Performance from the Nanoscale (CAMP-Nano), State Key Laboratory for Mechanical Behavior of Materials, Xi'an Jiaotong University, Xi'an, Shaanxi 710049, China
[b] Advanced Light Source, Lawrence Berkeley National Laboratory, Berkeley, CA 94720, USA

HIGHLIGHTS

- The heat affected zone cracking initiates due to the re-melting of preexisting intergranular γ/γ′ eutectics and coarse γ′.
- The transverse tensile strain/stress causing the initiation and propagation of crack is quantitatively measured.
- The micro-size MC carbides are considered to be a possible contributor to the hot cracking initiation.

GRAPHICAL ABSTRACT

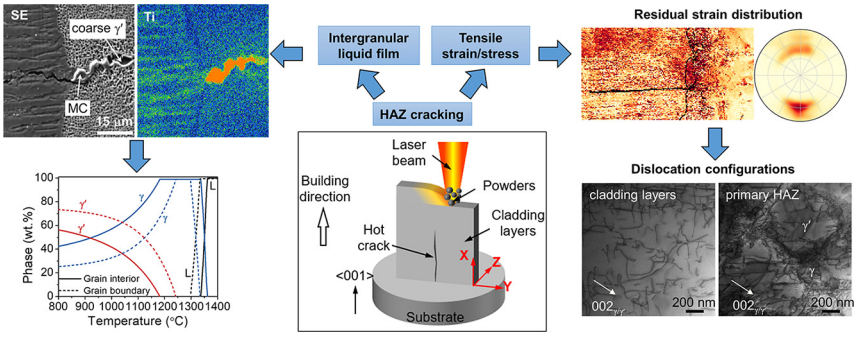

ARTICLE INFO

Article history:
Received 21 January 2018
Received in revised form 10 April 2018
Accepted 12 April 2018
Available online 14 April 2018

Keywords:
HAZ cracking
Laser 3D printing
Ni-based superalloy
Residual strain/stress
Synchrotron X-ray microdiffraction

ABSTRACT

Laser 3D printing is a promising technique to repair damaged Ni-based superalloy components. However, the occurrence of heat affected zone (HAZ) cracking severely limits its applicability. Here we unravel the cracking mechanism by studying the element, phase, defect, and strain distribution around an intergranular crack that initiated from the primary HAZ. Using synchrotron X-ray Laue microdiffraction, we measured high tensile strain/stress transverse to the building direction in both the primary HAZ and the cladding layers, as well as high-density dislocations, which resulted from the thermal contraction and rapid precipitation of γ′ phase. The crack initiated because the transverse tensile strain/stress tore up the liquid film formed by the low-melting point preexisting phases in the primary HAZ, such as γ/γ′ eutectics and coarse γ′ precipitates. The incoherent carbide particles were frequently observed near the crack root as local strain concentrators. In the cladding layers, micro-segregation could not be completely avoided, thus the hot crack continued to propagate over several layers with the assistance of the transverse tensile stress. Our investigations provide a useful guideline for the optimization of the 3D printing process to repair Ni-based superalloys with high susceptibility to hot cracking.

1. Introduction

Directionally solidified Ni-based superalloys, in which crystal grains grow preferentially along the ⟨001⟩ direction without transverse grain boundaries, have been widely applied in gas turbine engine components [1–3]. Ti and Al are the most commonly added elements to form the hardening phase — $L1_2$ ordered γ′-Ni_3(Al, Ti) precipitate, and improve the mechanical performance. However, it is widely recognized that once the combined amount of Al and Ti exceeds 6 wt%, the alloy becomes extremely susceptible to hot cracking in the heat affected zone (HAZ) during welding process due to the high stresses induced by rapid precipitation of the γ′ phase [4,5]. Besides, other refractory elements (REs) such as Nb, Ta, Re, Ru, and W are frequently employed to enhance

* Corresponding author.
E-mail address: kchenlbl@gmail.com (K. Chen).

https://doi.org/10.1016/j.matdes.2018.04.032
0264-1275/

the high-temperature property [1]. The segregation of these low-diffusivity REs leads to the formation of topologically close-packed phases [6] in the interdendritic regions and grain boundaries, potentially lowering the interfacial cohesion and cracking resistance. Besides the ductility-dip cracking resulting from severe ductility drop at intermediate temperatures [7], two other categories of hot cracking are also commonly observed:

1) Liquation cracking occurs when the thermal stress acts on the intergranular liquid film that is formed by the re-melting of as-cast constituents with low melting points such as γ/γ′ eutectic, coarse γ′, and metallic carbides (MC, M = Ti, W, Ta, Mo, Nb) [4,5,8], generating a gap in the microstructure that propagates as a crack.
2) Solidification cracking takes place when the liquid remaining along the grain boundaries or in the interdendritic regions fails to withstand the thermal stress in the final stage of solidification [9].

In both cases, thermal stress is believed to be the driving force for tearing the materials up. However, local strain/stress has been scarcely quantified in previous studies due to lack of characterization techniques, and thus a quantitative model is still yet to be proposed to fully understand the mechanism of cracking in the complex Ni-based superalloy material system during non-equilibrium solidification processes such as welding and metal additive manufacturing.

In recent years, laser additive manufacturing, also known as 3D printing, has showcased promising potentials for precise repair and rapid fabrication of Ni-based superalloy components [5,8,10]. However, hot cracks have been observed in the cladding layers, which is one of the greatest concerns for the application of this technique [5]. Due to the high solidification rate and the cyclic thermal loading accompanying the repeated layer-by-layer deposition, 3D printing produces finer dendrite and γ/γ′ networks [10–12], higher defect concentration [13], less element segregation [8,14], and different strain/stress distribution [15,16], when compared to conventional casting products. Consequently, accurate measurements of the microscopic strain, elemental segregation, and phase distribution in a laser 3D printed Ni-based superalloy are needed to understand the crack formation mechanism and to optimize the manufacturing parameters. In this study, a laser 3D printed Ni-based superalloy with combined weight concentration of Al and Ti exceeding 8% (Table 1) is investigated by a thorough microstructural characterization, combining the techniques of synchrotron X-ray Laue microdiffraction (μXRD), transmission electron microscopy (TEM), and electron probe microanalysis (EPMA). The fundamental mechanism of the hot crack initiation from the HAZ is unraveled, and possible approaches to crack prevention are discussed.

2. Experimental methods

The laser 3D printing was conducted using an independently developed XJTU-I additive manufacturing apparatus with a Nd:YAG laser source [17]. As shown in the schematic (Fig. 1a), the thin-walled sample was cladded by layers of ~100 μm on an as-cast DZ125L superalloy cylinder in the size of about 50 mm in diameter and 5 mm in height without any pre-processing heat treatment. The DZ125L alloy is a commonly used directionally solidified Ni-based superalloy for fabricating turbine blades and vanes in China [18]. As a surrogate of repairing the tip of turbine blade fabricated by directional solidification along ⟨001⟩ crystallographic direction, the repair surface chosen in this study was parallel to the (001) crystal plane of the substrate [19–21]. Each cladding layer was deposited by feeding gas-carried DZ125L superalloy powders into the melt pool generated by laser heating at the surface and protected from oxidation by an argon atmosphere. The detailed laser 3D printing parameters are listed in Table 2. When depositing a new layer, the adjacent as-deposited layer partly re-melted to form a strong metallurgical bond [22]. To distinguish the HAZs between two adjacent cladding layers from the one near the interface between cladding layers and substrate, the latter is denoted as the primary HAZ in this article. To describe the sample geometry, a Cartesian coordinate system **O-XYZ** is defined, as shown in Fig. 1a, with the **X**-axis parallel to the building direction, the **Y**-axis along the laser scanning direction.

Table 1
Nominal chemical compositions of the substrate and powder (wt%).

Material	Co	Cr	W	Al	Ta	Ti	Mo	C	B	Ni
Substrate	9.54	8.74	6.46	5.03	3.96	3.18	2.21	0.12	0.0076	Balance
Powder	9.64	9.70	7.14	4.90	3.78	3.12	2.18	0.09	0.015	Balance

After laser 3D printing, the sample was cut, mechanically ground with SiC sandpaper, and finely polished with ~0.5 μm diamond paste along the **XY**-plane. A microcrack close to the middle of cladding layers was observed along the **X**-direction under an optical microscope (OM, Carl Zeiss Axio Scope A1), as shown in Fig. 1b. Two platinum (Pt) markers were deposited with a focused ion beam (FIB, FEI Helios 600) system to facilitate positioning in the subsequent μXRD experiment. The morphological change of γ′ precipitate was investigated under scanning electron microscopy (SEM, Hitachi SU6600) in either secondary electron (SE) or backscattering electron (BSE) mode after electro-etching in aqueous phosphoric acid (30 vol%) at 5 V for 5 s. The elemental distributions near the root and tip of the crack were mapped respectively using EPMA (JEOL JXA-8100) with the acceleration voltage of 20 keV after slightly dissolving the γ′ precipitates using fresh nitro-hydrochloric acid.

The μXRD experiment was conducted on beamline 12.3.2 at the Advanced Light Source, Lawrence Berkeley National Laboratory [23]. The sample was placed at the focal point of the incident polychromatic X-ray beam (5–24 keV) and tilted 45° with respect to it. The accurate position of the Pt markers was detected using X-ray fluorescence signals. Afterward, a 450 × 240 μm^2 area on the sample surface, indicated by the blue dashed rectangle in Fig. 1b, was raster-scanned with the micro-focused X-ray beam (the beam size was about 1 × 1 μm^2). The scanning step sizes along the **X**- and **Y**-directions were 3 and 2 μm, respectively. Since columnar grain size was millimeters in length and hundreds of microns in width, much bigger than the polychromatic X-ray beam size, a Laue diffraction pattern was recorded in reflection mode using a DECTRIS Pilatus 1 M area detector at each scanning position. By fitting the Laue peaks to a 2D Gaussian function, the positions of all recorded peaks were obtained and the corresponding scattering vector **q** of each peak was calculated by subtracting the incident wave vector from the diffraction wave vector. A successful indexation was obtained by matching the angles between these **q** vectors with a pre-calculated list of theoretical angles between two crystal planes of a known unit cell within an angular tolerance. The initial indexing provided the crystal orientation matrix which could be used to deduce the theoretical position of each Laue peak. From the deviations between the measured and the theoretical peak positions, the changes in the relative length and angle between the lattice vectors were calculated at constant unit-cell volume, enabling the calculations of the deviatoric strain tensor at each position [24,25].

In order to evaluate the dislocation density under transmission electron microscope (TEM), a slice with a thickness of 800 μm was cut from the as-fabricated sample by electrical discharge machining and then ground into ~80 μm in thickness. Then a 3 mm diameter disc was punched out and finally thinned in a solution of 8% $HClO_4$ and 92% ethanol using a twin-jet electro-polishing machine. By controlling the size of the eroded hole in the center of the disc, the electron transparent area spanning from the substrate to cladding layers was obtained. Then dislocation observation and phase identification in the sample were conducted by a 200 kV JOEL 2100F TEM.

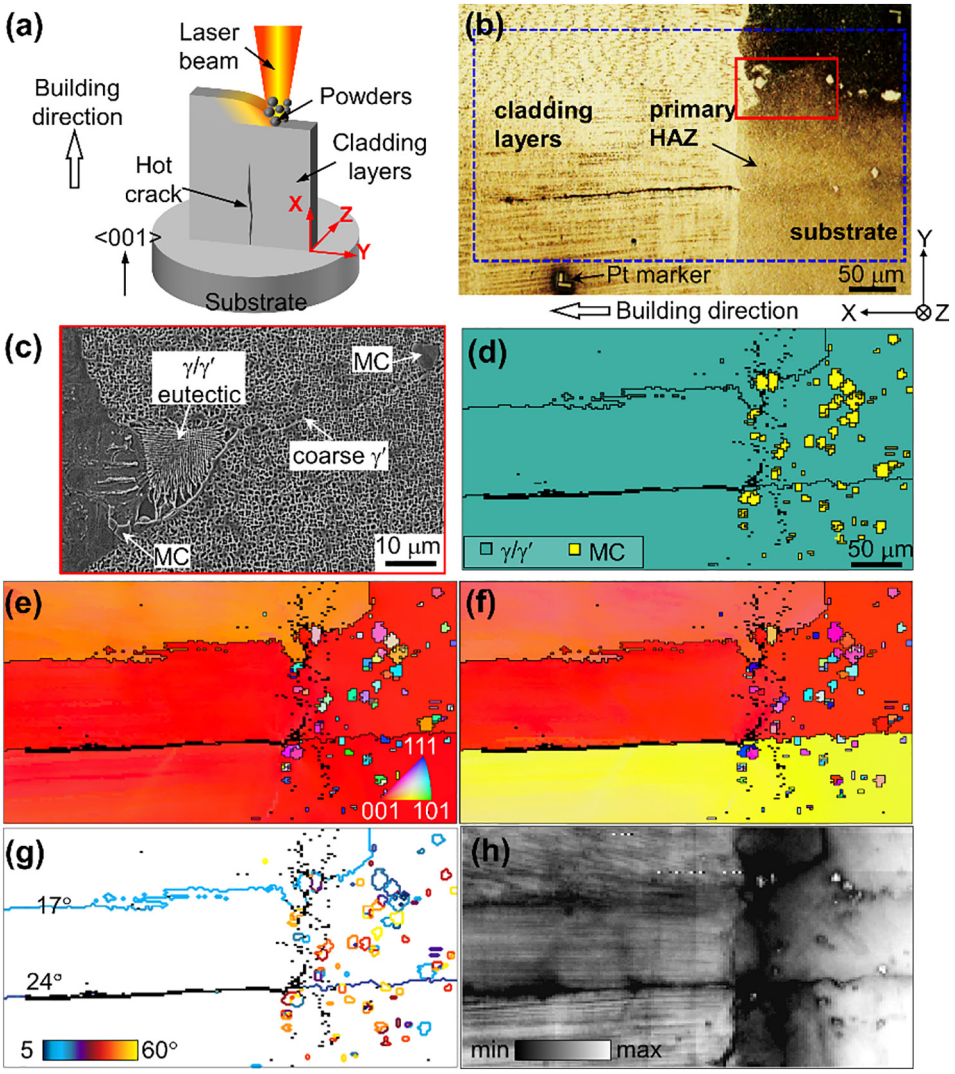

Fig. 1. (a) Schematic of laser 3D printing setup. (b) OM image of a hot crack region. (c) SE-SEM image of the region denoted by red rectangle in (b). (d) Phase distribution, (e–f) IPF maps along the **X**- and **Y**-directions, respectively, (g) grain/phase boundary misorientation, and (h) the filtered intensity map obtained by μXRD data from the area denoted as the blue rectangle in (b). The black pixels in the μXRD maps represent areas where the Laue patterns did not index, either because of material loss at the crack or severe plastic deformation in the primary HAZ. (For interpretation of the references to color in this figure legend, the reader is referred to the web version of this article.)

3. Results

3.1. Microstructural characterization near the crack region

In Fig. 1b, clearly visible in the cladding layers are the rapidly solidified fine dendrites, parallel to the building direction. Also visible is a crack that initiated at the primary HAZ/cladding interface and propagated along a grain boundary. Near an adjacent boundary a number of preexisting phases, including fan-like γ/γ′ eutectic, blocky metallic carbides and coarse γ′ particles are visible in the cast substrate (Fig. 1c). After indexing the Laue patterns using the peak position comparison method described elsewhere [26], the phase distribution in the sample is obtained, including γ/γ′ phase and B1 structure MC (M = Ta, Ti, W) type carbides with size ranging from 5 to 20 μm. More MC particles are observed in the μXRD map in Fig. 1d than in the optical micrograph in Fig. 1b. This is because high-energy synchrotron X-ray beam can penetrate over 40 μm deep in the alloy [15] and those MC particles beneath the sample surface can also be detected. It is seen that those MC particles possess distinct orientations (Fig. 1e and f) from the surrounding matrix. The misorientation angle between the MC particles and matrix ranges from 5 to 60° (Fig. 1g), implying the incoherent nature of the boundaries between MC particles and γ/γ′ phase [27,28]. Both of the two grain boundaries observed in the studied region are tilt grain boundaries, and the misorientation angles are about 24° and 17°, respectively. In addition, the uniform color of the inverse pole figure (IPF) maps along the building direction (Fig. 1e and f) indicate epitaxial growth of dendrites along the ⟨001⟩ direction in cladding layers with the assistance of steep thermal gradient during the 3D printing process [22,29]. For an overall view of microstructural features, the filtered diffraction intensity map (Fig. 1h) is obtained using a method introduced in details elsewhere [11]. The crack and grain boundaries are clearly visible. The bright contrast in the substrate suggests a low density of dislocations. In contrast, the primary HAZ, corresponding to the darker

Table 2
The technical parameters of laser 3D printing.

Parameter	Value
Laser power input	180 W
Scanning speed	10 mm/s
Laser beam diameter	~0.5 mm
Powder diameter	40–100 μm
Powder feed rate	4–5 g/min
Argon injection rate	4 L/min
Layer thickness	~100 μm

region in the intensity map, is characterized as a region with more defects [11]. The alternately bright and dark streaks in the cladding region are the dendrite core and interdendritic region, respectively. The latter one always contains higher dislocation density and serves as low angle grain boundaries [15].

Dislocation configurations in laser 3D printed Ni-based superalloy has been further observed using TEM. Fig. 2a shows that the ordered γ′ precipitates in the substrate have a cube-on-cube orientation relationship with the surrounding γ matrix, as suggested by the selective area electron diffraction (SAED) pattern displayed in the inset. Very few dislocations are visible, in agreement with the higher diffraction intensity in the substrate (Fig. 1h). However, in the primary HAZ (as shown in Fig. 2b–c), the dark shadow around the γ′ particle indicates an extremely high density of dislocations in this region. There are however fewer dislocations inside the γ′ particle. As a consequence, during the first-layer deposition process, a large population of dislocations activated by thermal stress is prominently anchored by the γ′ precipitates and thus piles up and forms dislocation networks at the γ/γ′ interface. The dislocation density is too high to be accurately determined by counting the individual dislocation lines. It should be emphasized that it is rather difficult to determine the exact distance from the TEM observation area to the HAZ/cladding interface. In contrast to dense dislocation tangles in the primary HAZ, the dislocations in cladding layers are less numerous and tend to be relatively straight, as shown in Fig. 2d. Consequently, the rapid cooling rate during laser 3D printing process subjects the primary HAZ and cladding layers to intense strain/stress levels resulting in high dislocation densities. Apparently, the number of dislocations observed in the primary HAZ (Fig. 2c) is more than an order of magnitude higher than that in the cladding layers (Fig. 2d). Although the thickness of these two observed areas may be different, the dislocation density in the primary HAZ is significantly higher than that in the cladding layers.

As reported in previous literature, solution cooling rate can effectively tailor the morphology and size distribution of γ′ precipitates [30–32] as well as the mechanical properties [12,32]. In our study, the morphological evolution of γ′ precipitates is shown in Fig. 3. In contrast to the mono-modal size distribution in the cast substrate (Fig. 3a and b), the γ′ precipitates in the primary HAZ feature a bimodal distribution (Fig. 3c and d). The primary γ′ precipitates (γ'_{1st}) become smaller and their number decreases substantially. Surrounding γ'_{1st}, a large population of tiny secondary γ′ precipitates (γ'_{2nd}) appears. During a thermal cycle, the γ'_{1st} partially or fully dissolves into the γ matrix once the local temperature exceeds its solvus and then re-precipitation from the supersaturated γ matrix takes place during the subsequent cooling process. The size of γ'_{2nd} precipitates is smaller than that of γ'_{1st} by an order of magnitude because of the faster cooling rate and short duration of the laser beam. In the cladding layers, the γ′ size (Fig. 3e and f) is close to the γ'_{2nd} size in the primary HAZ as a result of the similar cooling rate in the solid state. The non-uniform dislocation density is believed to be linked with the inhomogeneous γ′ size distribution. The big undissolved γ'_{1st} particles greatly inhibit the dislocation motion in the primary HAZ and thus dislocation pile-ups are observed at the γ/γ'_{1st} interface. In contrast, the dislocations are more mobile in the cladding layers because of the much smaller γ′ precipitates, and thus the dislocation density decreases as a result of dislocation annihilation and rearrangement. The segregation of γ′ former elements results in higher γ′ solvus and thus

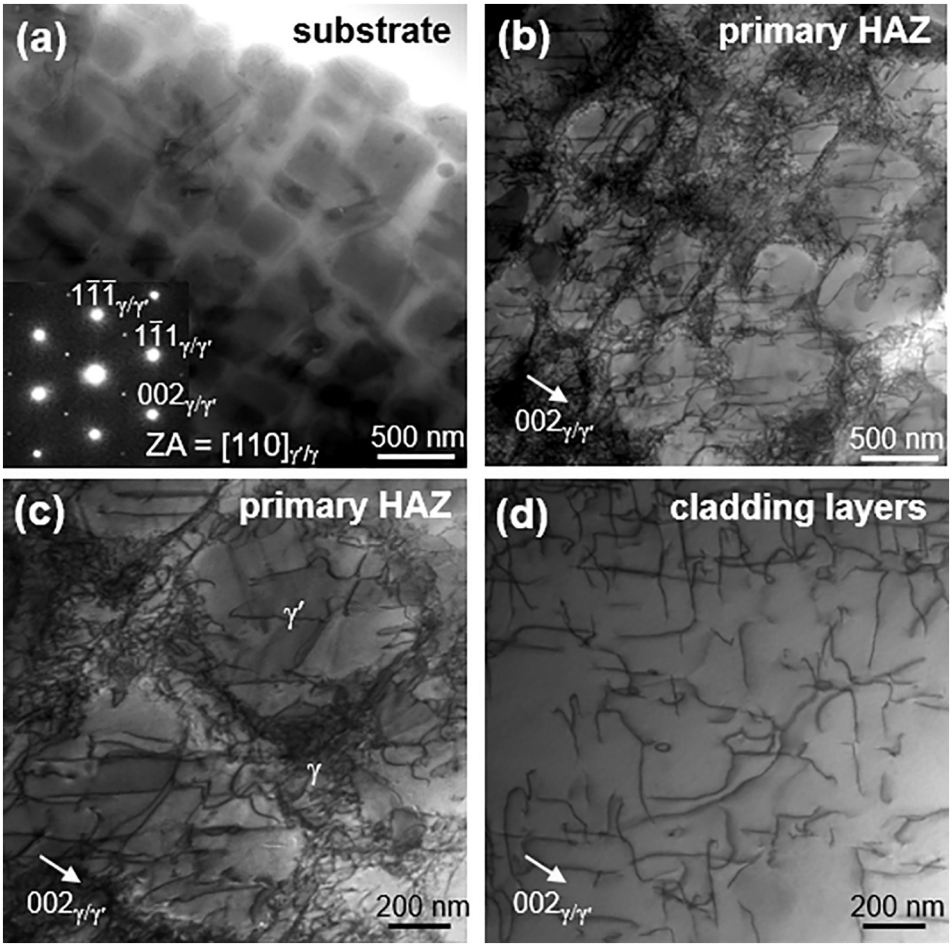

Fig. 2. (a) Cuboidal shape of γ′ precipitates in substrate investigated along the [011] direction. The corresponding diffraction pattern is shown in the inset. Dislocation structures observed in (b–c) the primary HAZ and (d) cladding layers. All the images are obtained under bright field STEM mode.

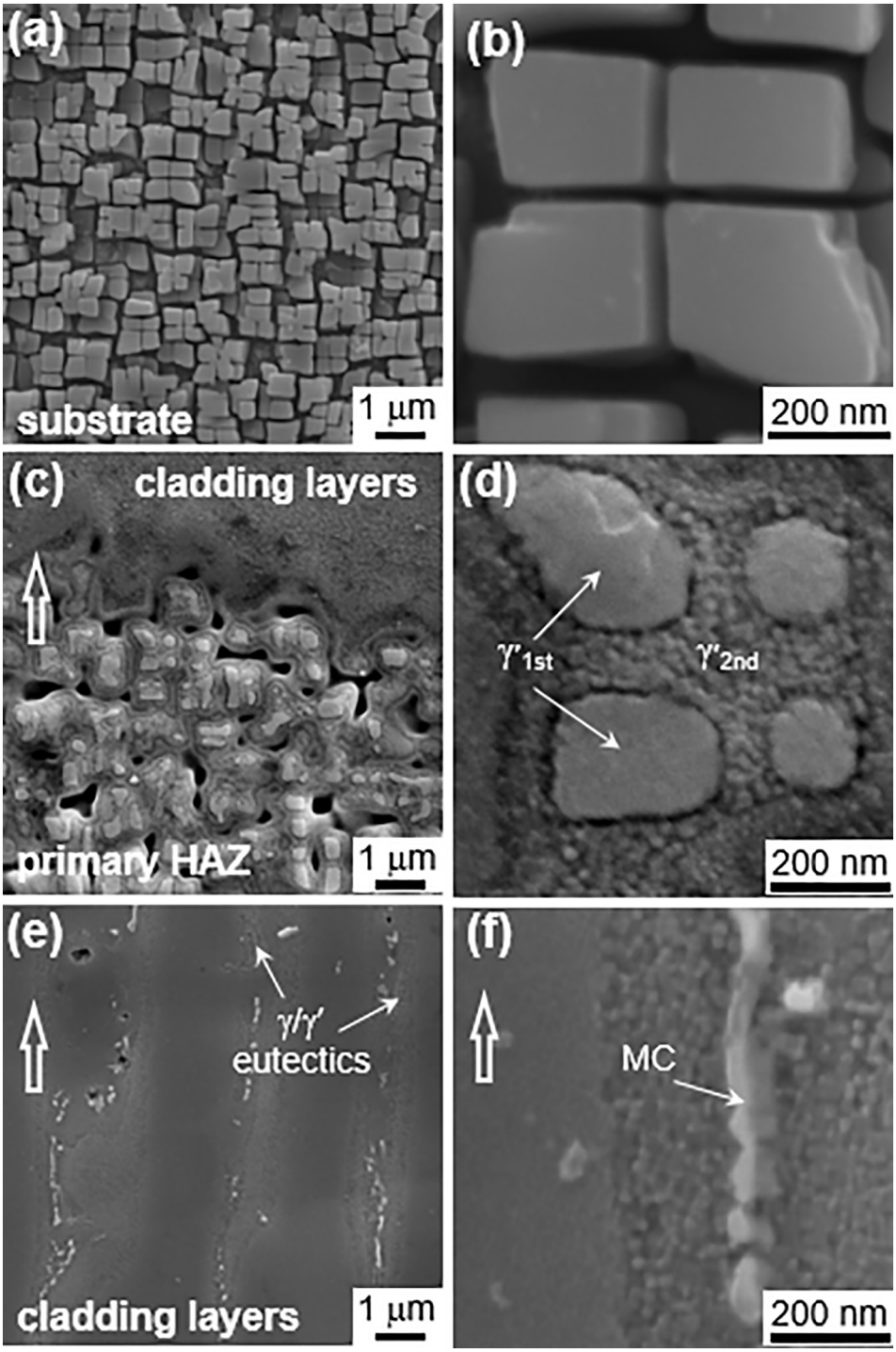

Fig. 3. Low and high magnification of SE-SEM images of typical morphologies of γ′ precipitates in (a–b) the substrate, (c–d) the HAZ/cladding interface, and (e–f) the cladding layers, respectively. The open arrows in white denote the building direction.

larger γ′ precipitates in the interdendritic region than in the dendrite core [33]. Solidification products, such as nano-sized carbides and fine γ/γ′ eutectics, are also observed. The more detailed characterization of structures and compositions of interdendritic carbides will be further discussed in the next section.

3.2. Elemental distribution near the crack region

The measured average primary dendrite arm spacing in cladding layers ranges from 3 to 5 μm, which is about two orders of magnitude smaller than in the substrate (~200 μm) due to the steep temperature gradient and fast cooling rate during the laser 3D printing process, indicating the interdendritic segregation in cladding layers are greatly suppressed [14]. Here, by using SEM and EPMA, the microstructure and element distribution near the root and tip are investigated and demonstrated in Figs. 4 and 5, respectively. In the primary HAZ (right half of Fig. 4), MC particles, rich in Ta and Ti as well as coarse γ′ precipitates, rich in Al, Ta, and Ti, are found near the crack root. By comparing the left half of Fig. 4 and the whole frame of Fig. 5, it is found that the element distribution at the crack tip is similar with the cladding regions near the crack root, as the morphology and size of γ′ precipitates. In the cladding layers, element segregation is detected and the interdendritic

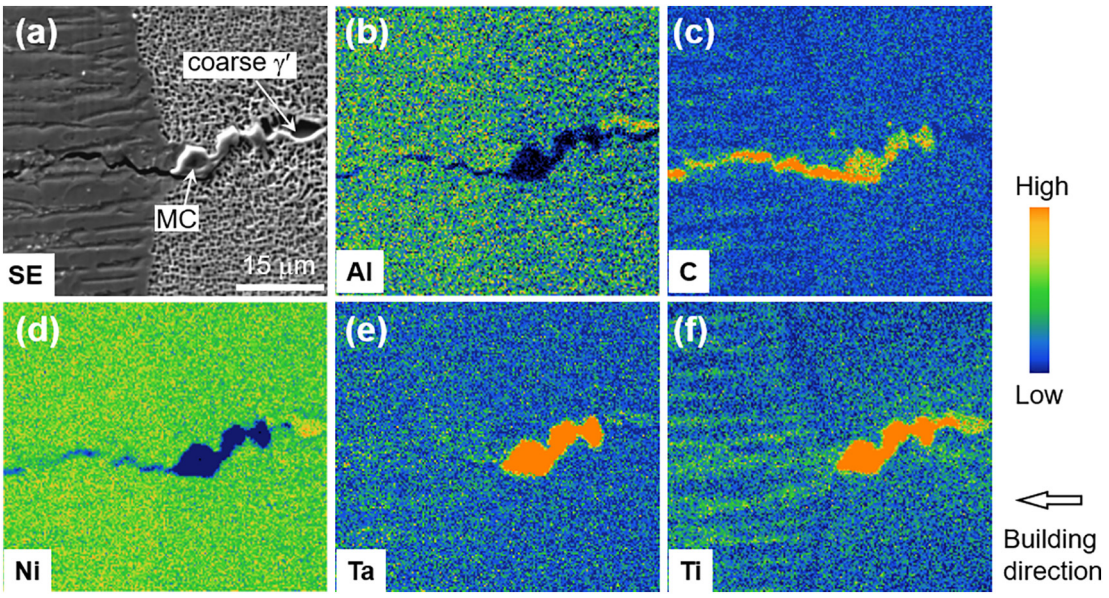

Fig. 4. (a) SE-SEM image and (b–f) element distributions near the crack root. The very high counts of C inside the crack in (c) resulted from remnant of polishing diamond paste, same as in Fig. 5(c).

regions are rich in C, Ta, and Ti. As listed in Table 3, the partition coefficients of these elements, which is defined as the compositional ratio in dendrite core to that in the interdendritic region, agree with the calculation by Ojo et al. [4]. Here, for comparison, the compositions and partition coefficients in the grain interior and boundary in primary HAZ are also respectively listed in Table 3. The intergranular segregation in the substrate is more severe than that in the interdendritic region in the cladding layers because of the different cooling rates. From the SE-SEM images in Figs. 4 and 5, the crack shows a relatively jagged trajectory, and a short crack is observed besides the main crack tip, which may be a branch of the main crack but beneath the sample surface so that it is not observed before etching in the optical micrograph.

During the last stage of solidification, the solute enrichment in the interdendritic region can produce different kinds of constituents, such as fine γ/γ′ eutectics and carbides (Fig. 3e). The carbides can nucleate heterogeneously above the liquidus temperature, and then start to grow, accompanied by the formation of γ phase [34]. Because of the high intrinsic hardness, the carbides are frequently found as a strong barrier for the dislocations induced by the intense thermal strain/stress, as seen in Fig. 6a. Similarly to the large carbides in the substrate, the interdendritic carbides are also identified as MC-type structure from the electron diffraction. Here two sets of diffraction patterns at different tilt angles are collected from the two MC particles. The different orientation relationships with the γ matrix indicate that the MC particles are randomly oriented relative to the γ matrix, in the same manner as in the substrate. Moreover, EDS maps (Fig. 6d–h) collected in the same area illustrate that these MC particles are rich in Mo, Ta, Ti and W. It is noted that no MC particles in cladding layers are probed from the μXRD maps in Fig. 1, because the high energy synchrotron X-ray beam penetrates deep into the material, thus the diffraction peak intensity

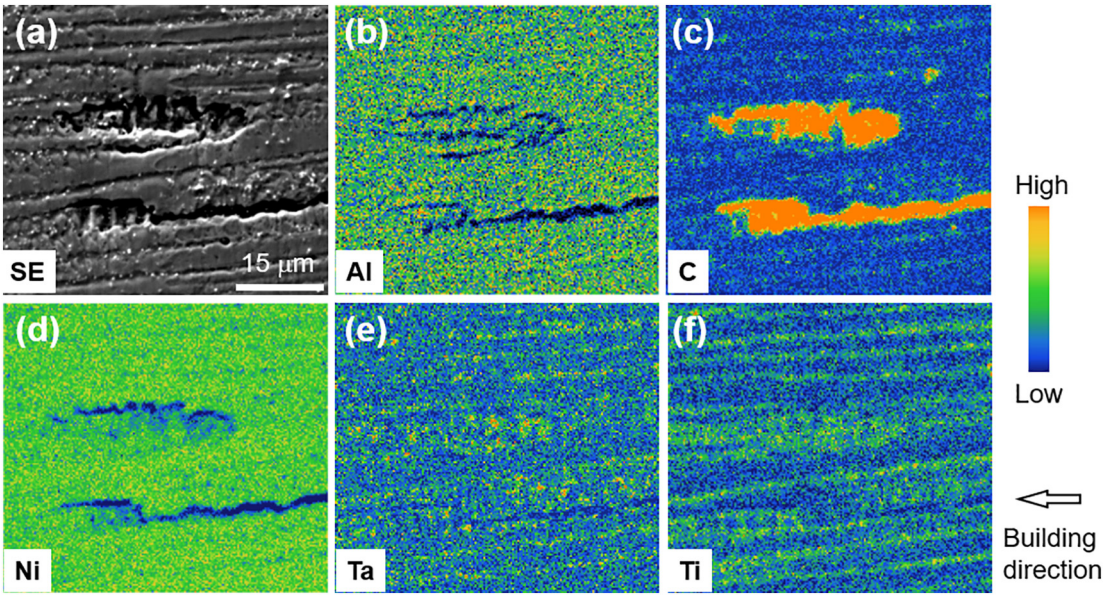

Fig. 5. (a) The SE-SEM image and (b–f) element distributions near the crack tip.

Table 3
Chemical compositions of the cladding layers and the cast substrate measured using EPMA.

Elements	Cladding layers			Primary HAZ		
	Dendrite core (wt%)	Interdendritic region (wt%)	Partition coefficient	Grain interior (wt%)	Grain boundary (wt%)	Partition coefficient
Co	9.84	9.18	1.07	10.25	8.84	1.15
Cr	9.45	8.77	1.08	8.90	6.89	1.29
W	7.72	7.00	1.10	7.92	4.21	1.88
Al	5.37	5.66	0.95	4.74	5.30	0.89
Ta	3.03	4.48	0.68	2.80	5.40	0.52
Ti	2.70	4.35	0.62	2.42	4.05	0.59
Mo	1.68	2.28	0.74	1.96	2.02	0.97
Ni	60.21	58.28	1.07	61.01	63.29	0.96

Note: light elements such as B, C are excluded due to the insufficient accuracy of EPMA.

from the nano-sized MC particles is much weaker than those from γ and γ′ phases.

4. Discussion

4.1. Grain boundary characteristics to crack susceptibility

Since grain boundary frequently shows strong susceptibility to hot cracking, it is necessary to specify the grain boundary characteristics for a comprehensive understanding of how the hot crack occurs. For this purpose, another sample with a HAZ crack is intentionally broken to examine the fracture surface, as shown in the schematic in Fig. 7a. Then the images of the fracture surface of the preexisting hot crack and the artificially generated crack in the primary HAZ are obtained by SEM as shown in Fig. 7b and c, respectively. As seen from Fig. 7b, a typical dendritic morphology accompanied with spherical drops are observed, giving evidence of the complete wetting of liquid film along the grain boundary in the primary HAZ [35]. However, the fracture surface of the artificial crack is typically flat and some traces and shear bands can be clearly seen from the inset in Fig. 7c [36]. By comparing Fig. 7b with Fig. 7c, it can be concluded that the crack initiated when the grain boundary was filled with a continuous liquid film, in other words, this is a strong indication of a typical liquation cracking mechanism.

The potential contributors to the intergranular liquid film are further discussed as follows. Frequently in the primary HAZ, as seen in Fig. 7d, the grain boundary, originally decorated by discrete coarse γ′ due to severe segregation of γ′ forming elements, re-melted and a liquid film formed during the first-layer deposition process. To evaluate the effect of elemental segregation on the solidification behavior, the thermodynamic software Jmatpro [37] is used to simulate the equilibrium phase diagrams (Fig. 8) based on the chemical compositions of the cladding layers and primary HAZ in Table 3, respectively. Since the contents of carbon and boron are low and hard to measure accurately, their effects on the phase diagram are negligible and thus only the liquid phase, γ matrix and γ′ precipitate are considered during the thermodynamic calculation. By using the database dedicated to nickel-based superalloy, the γ′ solvus, solidus and liquidus of different regions are obtained from the phase diagrams and listed respectively in Table 4. It is seen that the intergranular segregation raises the γ′ solvus, which means that intergranular γ′ starts to precipitate at higher temperature [33] and continues to coarsen following the well-known LSW theory [38]. In particular, the intergranular segregation can effectively suppress the melting point of the alloy, resulting in the formation of an intergranular liquid film (Fig. 7d) and the curved primary HAZ/cladding interface bending towards the HAZ (Figs. 1b and 7d). It should be noted that the simulation results may deviate from reality and the solidification path is complex due to the complicated chemical compositions of the Ni-based superalloy and the intrinsic non-equilibrium solidification process of laser 3D printing. However, the local composition based simulation results still provide a useful reference for investigating the melting or solidification sequence in order to discuss the contributors to the

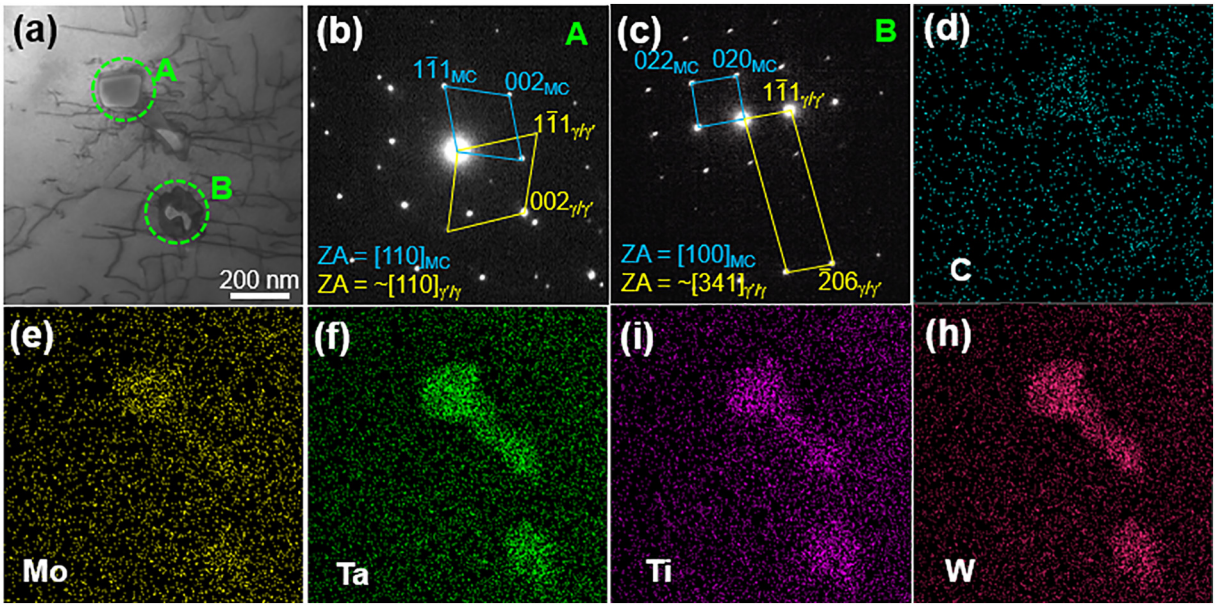

Fig. 6. TEM characterization of interdendritic carbides in the cladding layers. (a) Bright field STEM image; (b–c) the corresponding electron diffraction patterns collected from the areas A and B denoted in (a). (d–h) EDS maps of C, Mo, Ta, Ti and W, respectively.

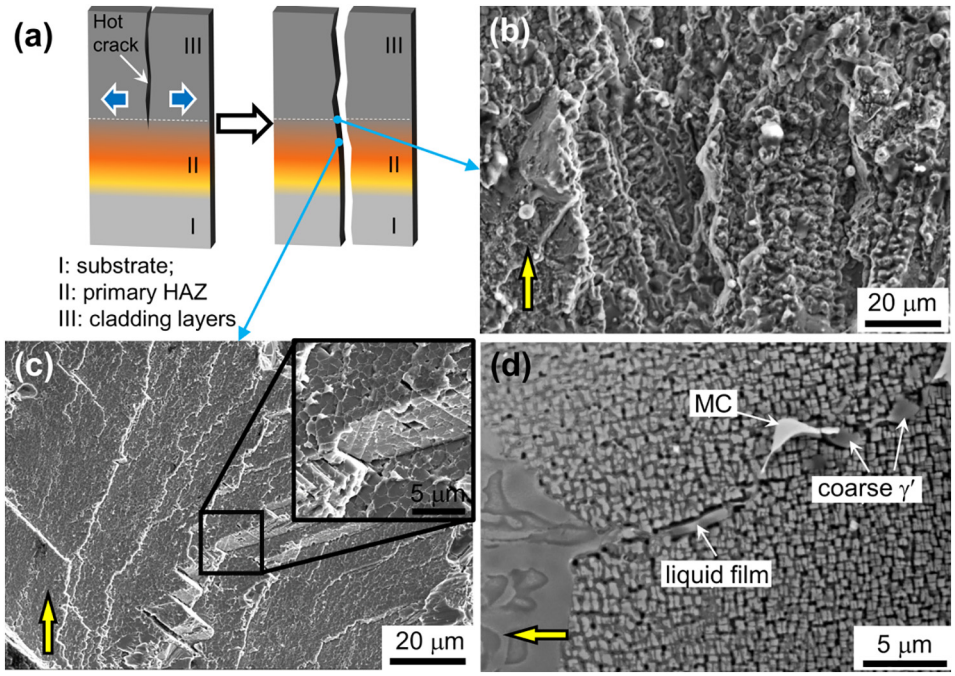

Fig. 7. (a) Schematic of fractographic study of the hot cracking. The SE-SEM images of facture surfaces of (b) the root of hot cracking and (c) artificial crack in the primary HAZ. (d) BSE-SEM image shows a typical grain boundary morphology in the primary HAZ. The arrows in (b–d) denote the building direction.

intergranular liquid. In contrast to previous studies [4,8], micro-sized MC particles, as shown in Fig. 1c, still persist in the cladding layers, proving that they have little contribution to the intergranular liquid film. Therefore, for the superalloy in this study, the γ/γ′ eutectic (Fig. 1c) and coarse γ′ precipitates (Fig. 7d) are conceived to be the main contributors to grain boundary liquation. The contribution to liquid film by intergranular γ′ is also comprehensively highlighted by Ojo et al. during the pre-weld heat treatment of cast Inconel 718 superalloy [33]. Overall, these preexisting low melting point phases and severe segregation along grain boundary promote the susceptibility to hot cracking in the primary HAZ.

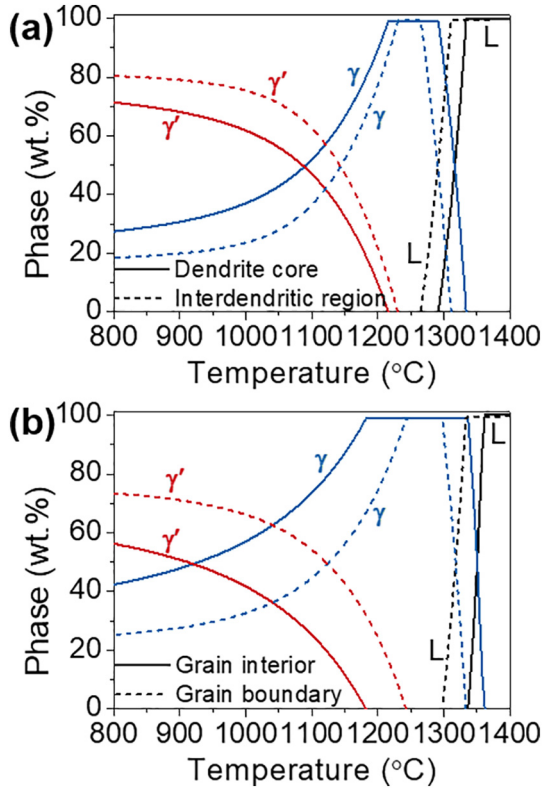

Fig. 8. Thermodynamic calculation of phase diagrams based on the chemical compositions of (a) the cladding layers and (b) the primary HAZ listed in Table 3, respectively.

Rappaz et al. [39] developed a theoretical model and proposed that the crack susceptibility of a grain boundary is related to the grain boundary energy, which controls the coalescence behavior of dendrites on both sides of the grain boundary. After a series of experiments, it is found that the grain boundary is likely to crack if the misorientation angle exceeded a critical value θ_c, which is dependent on temperature and chemical composition. Wang et al. [40] proposed that the θ_c was ~13°, while the values such as 15° and 16° were also reported by Chauvet et al. [35] and Rong et al. [41], respectively. The uncracked grain boundary misorientation (17°) is close to the reported values, thus it is not easy to tell if the uncracked grain boundary is a high angle grain boundary. Besides, the uncracked grain boundary is identified as a random grain boundary while the cracked one is a Σ13 boundary (22.6°/⟨001⟩). Thus, it is not easy to compare the energy of these two grain boundaries.

On the other hand, it should be emphasized that all the theories and mechanisms reported so far are about the 'susceptibility' of crack formation. In other words, it is by no means trivial to predict if a hot crack will initiate along a certain grain boundary or not, even if the misorientation and sigma value is known. What is more, hot cracks formation during the laser 3D printing process is affected by not only the grain boundary energy, but also a large number of other complicated factors, such as the

Table 4
Thermodynamic calculations based on the chemical compositions listed in Table 3.

Temperature	Cladding layers		Primary HAZ	
	Dendrite core (°C)	Interdendritic region (°C)	Grain interior (°C)	Grain boundary (°C)
γ′ solvus	1215	1230	1182	1243
Solidus	1291	1265	1336	1297
Liquidus	1334	1311	1362	1333

laser power and speed, unpredictable defects in the substrate and powders, and so on.

4.2. The driving force for crack initiation and propagation

During the cooling process, the thermal contraction and solidification shrinkage accompanied by rapid precipitation of γ′ in the primary HAZ and the cladding layers induce high strain/stress and severe elastic/plastic deformation. Although it is difficult to capture the thermal strain/stress evolution during 3D printing, the residual deviatoric strain in this region can be quantified using the μXRD technique [15,42]. As shown in Fig. 9, the magnitude and direction of compressive and tensile principal strains are calculated from the deviatoric strain tensors, respectively. The strains in the substrate are relatively low and homogeneous, but much more inhomogeneous strains are observed in the cladding layers with particularly large strain concentration near the interdendritic regions, because the dislocation movement is greatly retarded by the interdendritic phases, especially nano-sized MC particles. As a consequence, the susceptibility to cracking may get more pronounced due to the difficulty of dislocation movements [43]. The primary HAZ is subjected to a significantly higher strain state, and a clearly decreasing strain gradient from the HAZ/cladding interface to deep inside the substrate is visible. Therefore it is believed that the impingement between the laser beam and substrate generates intense strain/stress in the primary HAZ at the onset of the laser 3D printing process. It should be noted that there is also high strain concentration (Fig. 9a and b) near the MC particles in the substrate, which means that the incoherent MC particles can strongly introduce microstructural inhomogeneity to their surrounding matrix. Due to the high intrinsic hardness and brittle nature, micro-cracking initiates frequently in a high-stress environment, in the form of decohesion of carbides/matrix interface or breaking of the brittle MC carbides [44]. Besides, the diffusion of Ti from the γ′ precipitates to the MC particles during heat treatment usually results in the γ′ precipitate free zones (PFZs) near the carbides, where dislocation generation is promoted, and thus the resultant dislocation pile-ups give rise to the reduction of strength of superalloy [45]. Consequently, MC particles may serve as weak points for the resistance to hot cracking and they are frequently found near the crack root (Fig. 4).

High principal strain (±0.6%) in the laser 3D printed specimen is measured, due to the thermal contraction and rapid precipitation of γ′ phase. From Fig. 9c and d, the residual strain axis distributions in the primary HAZ and the cladding layers are quite similar. Most of the compressive strain axes align with the dendrite growth direction, while tensile strain axes are almost parallel to the cladding layers, in agreement with a previous study [15] regardless of the sample mounting direction, suggesting that the residual strain distribution is intrinsically a consequence of the layer-by-layer deposition and grain boundaries have little influence upon the strain direction.

As earlier mentioned, the morphology of γ'_{1st} precipitates in primary HAZ depends on the distance to the HAZ/cladding interface. And the change of γ'_{1st} shape and geometry due to partial dissolution may influence the γ/γ′ misfit, which is likely to create the misfit dislocation networks at the γ/γ′ interface [46]. Besides, the undissolved large γ'_{1st} precipitates are still strong impediments to dislocations. Therefore, the combination of the gradually changing γ′ size and work hardening by dislocation forests significantly increase the hardness of primary HAZ and cladding layers [12], which enormously degrades the resistance of

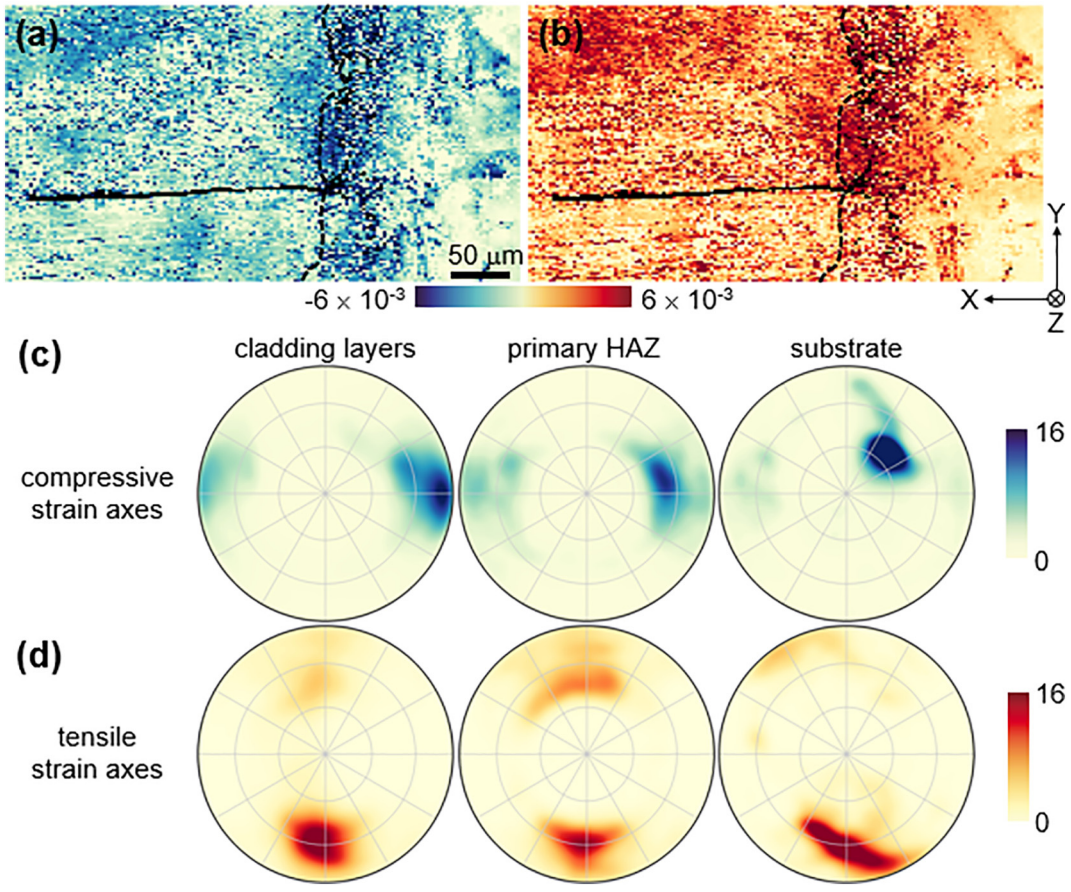

Fig. 9. The magnitude of principal (a) compressive and (b) tensile strain, respectively and the corresponding directions of (c) compressive and (d) tensile strain axes in the cladding layers, the primary HAZ and the substrate represented as stereographic projections with density contouring respectively.

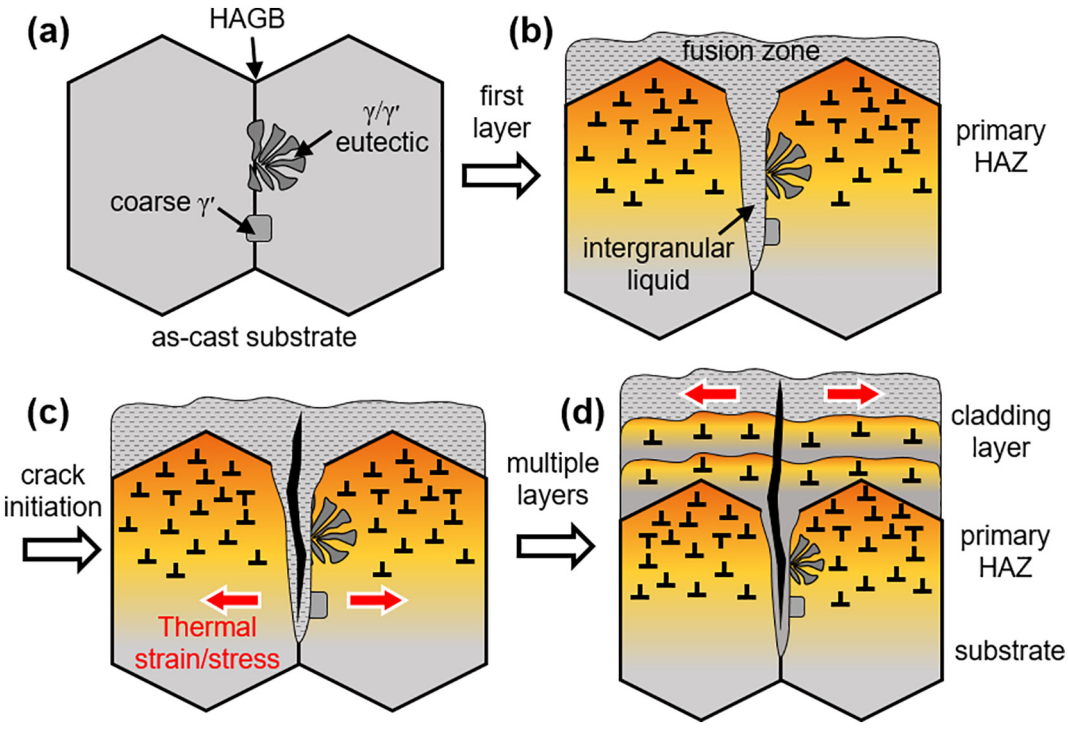

Fig. 10. The schematic showing the mechanism of intergranular hot cracking initiated from the primary HAZ.

HAZ cracking because a substrate with relatively higher hardness is bad for thermal stress/strain relaxation and will increase the stress burden and the driving force for intergranular cracking in HAZ [47].

4.3. Mechanisms of HAZ cracking initiation and propagation

By considering the element, phase, and strain distribution together, the crack initiation and propagation mechanism is demonstrated schematically in Fig. 10. Due to the slow solidification rate, γ′ forming elements had a high tendency to segregate along the grain boundary of the cast substrate, inducing the formation of intergranular constituents with low melting points, such as coarse γ′ and γ/γ′ eutectics. When depositing the first layer during laser 3D printing process, some of the low melting point phases in primary HAZ re-melted to form an intergranular liquid film, which drastically aggravated the grain boundary strength, especially those boundaries with high misorientation angles. Simultaneously, intense tensile strain/stress perpendicular to the building direction generated due to the fast solidification contraction and rapid re-precipitation of secondary γ′. Once the tensile stress transcended the degraded grain boundary strength, decohesion occurred and the crack initiated from the primary HAZ. At the same time, a number of dislocations were activated by the intense thermal stress in the primary HAZ. During the subsequent 3D printing process, micro-segregation could not be avoided, thus a thin liquid film existed along the grain boundary and interdendritic region at the final stage of the solidification of each deposited layer, forming the low-melting point phases, which can also be re-melted when the next layer was deposited. Therefore, the hot crack continued to propagate with the assistance of the tensile stress transverse to the dendrite growth direction. As a result, it is confirmed that the HAZ cracking initiated as liquation cracking; however, based on the present observations, it is difficult to identify whether the existing crack propagated as a liquation crack or a solidification crack in the layer-by-layer cladded materials due to the complex solidification path, including melting, re-melting, partial re-melting, cyclic annealing, etc. [35].

Since the co-occurrence of intergranular liquid film and intense thermal strain/stress is indispensable to the initiation of HAZ cracking, minimizing or even eliminating the preexisting cracking promoters in the cast substrate and reducing the thermal strain/stress during the 3D printing process are the key points to prevent cracking. To achieve this, a high-temperature heat treatment even above the γ′ solvus is required to dissolve the low-melting point crack promoters and homogenize the distribution of REs. Moreover, since the magnitude of thermal stress is proportional to the temperature gradient in HAZ [47], approaches to lowering the temperature gradient are favored for hot cracking reduction during the laser 3D printing process, such as preheating the substrate [48,49] and lowering the heat input [50].

5. Conclusions

The element, phase, strain, and defect distributions around an intergranular crack in Ni-based superalloy DZ125L fabricated by laser 3D printing technique are studied in detail using synchrotron μXRD, TEM, and EPMA. The γ/γ′ eutectics, coarse γ′ precipitates and the severe intergranular segregation contribute to the formation of an intergranular liquid film in the primary HAZ at the beginning of the laser 3D printing process. Simultaneously, intense in-plane tension induced by thermal contraction and re-precipitation of secondary γ′ activates high density of dislocations at the γ/γ′ interface, and further separates the liquid film from grain boundary in the primary HAZ. The resulting liquation cracking acts as the initiator of the extended cracking during the subsequent laser 3D printing process with the assistance of transverse tensile strain/stress. In the deposited materials, the in-plane tension sustains the crack propagation along the high angle grain boundary across several cladding layers. Based on our observations, it is concluded that proper pre-repair heat treatment on substrate and lowering of the thermal stress during 3D printing process will be useful to suppress crack formation.

Acknowledgments

This work is supported by the National Natural Science Foundation of China (Grant No. 51671154, 51405507), the National Key Research and Development Program (Grant No. 2016YFB0700404), the National

Basic Research Program of China ("973" Program) (Grant No. 2015CB057400), the International Joint Laboratory for Micro/Nano Manufacturing and Measurement Technologies, and the Collaborative Innovation Center of High-End Manufacturing Equipment. We appreciate the technical support from Mr. L.C. Huang and Mr. P.J. Yang (Xi'an Jiaotong University) for the FIB experiments, Ms. D.L. Zhang (Xi'an Jiaotong University) for the TEM characterization and Mr. N.C. Zhou (Xi'an Center of Geological Survey, China Geological Survey) for the EPMA tests. This research used beamline 12.3.2 at the Advanced Light Source, the CORI supercomputer at NERSC and the XMAS computational cluster resource managed by the IT Division's Scientific Computing Group, which are Lawrence Berkeley National Laboratory facilities supported by the DOE Office of Science User Facility under contract no. DE-AC02-05CH11231.

Data availability

The raw/processed data required to reproduce these findings cannot be shared at this time as the data also forms part of an ongoing study.

References

[1] T.M. Pollock, Alloy design for aircraft engines, Nat. Mater. 15 (2016) 809–815.
[2] T.M. Pollock, S. Tin, Nickel-based superalloys for advanced turbine engines: chemistry, microstructure and properties, J. Propuls. Power 22 (2006) 361–374.
[3] L. Liu, T. Huang, M. Qu, G. Liu, J. Zhang, H. Fu, High thermal gradient directional solidification and its application in the processing of nickel-based superalloys, J. Mater. Process. Technol. 210 (2010) 159–165.
[4] O.A. Ojo, N.L. Richards, M.C. Chaturvedi, Study of the fusion zone and heat-affected zone microstructures in tungsten inert gas-welded INCONEL 738LC superalloy, Metall. Mater. Trans. A 37 (2006) 421–433.
[5] Y. Chen, K. Zhang, J. Huang, S.R.E. Hosseini, Z. Li, Characterization of heat affected zone liquation cracking in laser additive manufacturing of Inconel 718, Mater. Des. 90 (2016) 586–594.
[6] C.M.F. Rae, R.C. Reed, The precipitation of topologically close-packed phases in rhenium-containing superalloys, Acta Mater. 49 (2001) 4113–4125.
[7] D. Qian, J. Xue, A. Zhang, Y. Li, N. Tamura, Z. Song, K. Chen, Statistical study of ductility-dip cracking induced plastic deformation in polycrystalline laser 3D printed Ni-based superalloy, Sci. Rep. 7 (2017) 2859.
[8] M. Zhong, H. Sun, W. Liu, X. Zhu, J. He, Boundary liquation and interface cracking characterization in laser deposition of Inconel 738 on directionally solidified Ni-based superalloy, Scr. Mater. 53 (2005) 159–164.
[9] M. Pakniat, F.M. Ghaini, M.J. Torkamany, Hot cracking in laser welding of Hastelloy X with pulsed Nd: YAG and continuous wave fiber lasers, Mater. Des. 106 (2016) 177–183.
[10] M. Gäumann, S. Henry, F. Cléton, J.-D. Wagnière, W. Kurz, Epitaxial laser metal forming: analysis of microstructure formation, Mater. Sci. Eng. A 271 (1999) 232–241.
[11] G. Zhou, W. Zhu, H. Shen, Y. Li, A. Zhang, N. Tamura, K. Chen, Real-time microstructure imaging by Laue microdiffraction: a sample application in laser 3D printed Ni-based superalloys, Sci. Rep. 6 (2016), 28144.
[12] D. Qian, A. Zhang, J. Zhu, Y. Li, W. Zhu, B. Qi, N. Tamura, D. Li, Z. Song, K. Chen, Hardness and microstructural inhomogeneity at the epitaxial interface of laser 3D-printed Ni-based superalloy, Appl. Phys. Lett. 109 (2016), 101907.
[13] J. Xue, A. Zhang, Y. Li, D. Qian, J. Wan, B. Qi, N. Tamura, Z. Song, K. Chen, A synchrotron study of microstructure gradient in laser additively formed epitaxial Ni-based superalloy, Sci. Rep. 5 (2015), 14903.
[14] Y.-J. Liang, J. Li, A. Li, X.-T. Pang, H.-M. Wang, Solidification path of single-crystal nickel-base superalloys with minor carbon additions under laser rapid directional solidification conditions, Scr. Mater. 127 (2017) 58–62.
[15] Y. Li, D. Qian, J. Xue, J. Wan, A. Zhang, N. Tamura, Z. Song, K. Chen, A synchrotron study of defect and strain inhomogeneity in laser-assisted three-dimensionally-printed Ni-based superalloy, Appl. Phys. Lett. 107 (2015), 181902.
[16] C. Casavola, S.L. Campanelli, C. Pappalettere, Preliminary investigation on distribution of residual stress generated by the selective laser melting process, J. Strain Anal. Eng. Des. 44 (2009) 93–104.
[17] X. Do, D. Li, A. Zhang, B. He, H. Zhang, T. Doan, Investigation on multi-track multi-layer epitaxial growth of columnar crystal in direct laser forming, J. Laser Appl. 25 (2013), 012007.
[18] Y. Zhang, Z. Xu, J. Xing, D. Zhu, Effect of tube-electrode inner diameter on electrochemical discharge machining of nickel-based superalloy, Chin. J. Aeronaut. 29 (2016) 1103–1110.
[19] M. Gäumann, C. Bezençon, P. Canalis, W. Kurz, Single-crystal laser deposition of superalloys: processing–microstructure maps, Acta Mater. 49 (2001) 1051–1062.
[20] L. Li, Repair of directionally solidified superalloy GTD-111 by laser-engineered net shaping, J. Mater. Sci. 41 (2006) 7886–7893.
[21] R. Vilar, A. Almeida, Repair and manufacturing of single crystal Ni-based superalloys components by laser powder deposition—a review, J. Laser Appl. 27 (2015), S17004.
[22] N.J. Harrison, I. Todd, K. Mumtaz, Reduction of micro-cracking in nickel superalloys processed by Selective Laser Melting: a fundamental alloy design approach, Acta Mater. 94 (2015) 59–68.
[23] M. Kunz, N. Tamura, K. Chen, A.A. MacDowell, R.S. Celestre, M.M. Church, S. Fakra, E.E. Domning, J.M. Glossinger, J.L. Kirschman, G.Y. Morrison, D.W. Plate, B.V. Smith, T. Warwick, V.V. Yashchuk, H.A. Padmore, E. Ustundag, A dedicated superbend x-ray microdiffraction beamline for materials, geo-, and environmental sciences at the advanced light source, Rev. Sci. Instrum. 80 (2009), 035108.
[24] J.S. Chung, G.E. Ice, Automated indexing for texture and strain measurement with broad-bandpass X-ray microbeams, J. Appl. Phys. 86 (1999) 5249–5255.
[25] N. Tamura, XMAS: a versatile tool for analyzing synchrotron x-ray microdiffraction data, in: R. Barabash, G. Ice (Eds.), Strain and Dislocation Gradients from Diffraction: Spatially-Resolved Local Structure and Defects, World Scientific, London 2014, pp. 125–155.
[26] J. Kou, K. Chen, N. Tamura, A peak position comparison method for high-speed quantitative Laue microdiffraction data processing, Scr. Mater. 143 (2018) 49–53.
[27] R.C. Reed, The Superalloys: Fundamentals and Applications, Cambridge university press, 2008.
[28] Y. Li, L. Wan, K. Chen, A look-up table based approach to characterize crystal twinning for synchrotron X-ray Laue microdiffraction scans, J. Appl. Crystallogr. 48 (2015) 747–757.
[29] T.T. Roehling, S.S.Q. Wu, S.A. Khairallah, J.D. Roehling, S.S. Soezeri, M.F. Crumb, M.J. Matthews, Modulating laser intensity profile ellipticity for microstructural control during metal additive manufacturing, Acta Mater. 128 (2017) 197–206.
[30] P.M. Sarosi, B. Wang, J.P. Simmons, Y. Wang, M.J. Mills, Formation of multimodal size distributions of γ′ in a nickel-base superalloy during interrupted continuous cooling, Scr. Mater. 57 (2007) 767–770.
[31] J. Tiley, G.B. Viswanathan, R. Srinivasan, R. Banerjee, D.M. Dimiduk, H.L. Fraser, Coarsening kinetics of γ′ precipitates in the commercial nickel base Superalloy René 88 DT, Acta Mater. 57 (2009) 2538–2549.
[32] R.J. Mitchell, M. Preuss, S. Tin, M.C. Hardy, The influence of cooling rate from temperatures above the γ′ solvus on morphology, mismatch and hardness in advanced polycrystalline nickel-base superalloys, Mater. Sci. Eng. A 473 (2008) 158–165.
[33] O.A. Ojo, N.L. Richards, M.C. Chaturvedi, Contribution of constitutional liquation of gamma prime precipitate to weld HAZ cracking of cast Inconel 738 superalloy, Scr. Mater. 50 (2004) 641–646.
[34] J. Li, H.M. Wang, Microstructure and mechanical properties of rapid directionally solidified Ni-base superalloy Rene′41 by laser melting deposition manufacturing, Mater. Sci. Eng. A 527 (2010) 4823–4829.
[35] E. Chauvet, P. Kontis, E.A. Jägle, B. Gault, D. Raabe, C. Tassin, J.-J. Blandin, R. Dendievel, B. Vayre, S. Abed, G. Martin, Hot cracking mechanism affecting a non-weldable Ni-based superalloy produced by selective electron Beam Melting, Acta Mater. 142 (2018) 82–94.
[36] Z. Zhang, G. Obasis, R. Morana, M. Preuss, Hydrogen assisted crack initiation and propagation in a nickel-based superalloy, Acta Mater. 113 (2016) 272–283.
[37] N. Saunders, U.K.Z. Guo, X. Li, A.P. Miodownik, J.-P. Schillé, Using JMatPro to model materials properties and behavior, JOM 55 (2003) 60–65.
[38] I.M. Lifshitz, V.V. Slyozov, The kinetics of precipitation from supersaturated solid solutions, J. Phys. Chem. Solids 19 (1961) 35–50.
[39] M. Rappaz, A. Jacot, W.J. Boettinger, Last-stage solidification of alloys: theoretical model of dendrite-arm and grain coalescence, Metall. Mater. Trans. A 34 (2003) 467–479.
[40] N. Wang, S. Mokadem, M. Rappaz, W. Kurz, Solidification cracking of superalloy single- and bi-crystals, Acta Mater. 52 (2004) 3173–3182.
[41] P. Rong, N. Wang, L. Wang, R.N. Yang, W.J. Yao, The influence of grain boundary angle on the hot cracking of single crystal superalloy DD6, J. Alloys Compd. 676 (2016) 181–186.
[42] R. Li, Q. Xie, Y.-D. Wang, W. Liu, M. Wang, G. Wu, X. Li, M. Zhang, Z. Lu, C. Geng, T. Zhu, Unraveling submicron-scale mechanical heterogeneity by three-dimensional X-ray microdiffraction, Proc. Natl. Acad. Sci. U. S. A. 115 (2018) 483–488.
[43] X. Wang, L.N. Carter, B. Pang, M.M. Attallah, M.H. Loretto, Microstructure and yield strength of SLM-fabricated CM247LC Ni-superalloy, Acta Mater. 128 (2017) 87–95.
[44] Q.Z. Chen, C.N. Jones, D.M. Knowles, The grain boundary microstructures of the base and modified RR 2072 bicrystal superalloys and their effects on the creep properties, Mater. Sci. Eng. A 385 (2004) 402–418.
[45] T. Krol, D. Baither, E. Nembach, The formation of precipitate free zones along grain boundaries in a superalloy and the ensuing effects on its plastic deformation, Acta Mater. 52 (2004) 2095–2108.
[46] M. Lachowicz, W. Dudziński, M. Podrez-Radziszewska, TEM observation of the heat-affected zone in electron beam welded superalloy Inconel 713C, Mater. Charact. 59 (2008) 560–566.
[47] A.T. Egbewande, R.A. Buckson, O.A. Ojo, Analysis of laser beam weldability of Inconel 738 superalloy, Mater. Charact. 61 (2010) 569–574.
[48] Q. Li, X. Lin, F. Liu, F. Liu, W. Huang, Microstructural characteristics and mechanical properties of laser solid formed K465 superalloy, Mater. Sci. Eng. A 700 (2017) 649–655.
[49] M. Ramsperger, R.F. Singer, C. Körner, Microstructure of the nickel-base superalloy CMSX-4 fabricated by selective electron beam melting, Metall. Mater. Trans. A 47 (2016) 1469–1480.
[50] G. Bi, C.-N. Sun, H. Chen, F.L. Ng, C.C.K. Ma, Microstructure and tensile properties of superalloy IN100 fabricated by micro-laser aided additive manufacturing, Mater. Des. 60 (2014) 401–408.